

# Spin Polarization in $\gamma d \rightarrow \vec{n}p$ at Low Energies with a Pionless Effective Field Theory

S.-I. Ando,<sup>1</sup> Y.-H. Song,<sup>2</sup> C. H. Hyun,<sup>1</sup> and K. Kubodera<sup>2</sup>

<sup>1</sup>*Department of Physics Education, Daegu University,  
Gyeongsan 712-714, Republic of Korea*

<sup>2</sup>*Department of Physics and Astronomy,  
University of South Carolina, Columbia, SC 29208, USA*

(Dated: May 14, 2011)

## Abstract

With the use of pionless effective field theory including dibaryon fields, we study the  $\gamma d \rightarrow \vec{n}p$  reaction for the laboratory photon energy  $E_\gamma^{lab}$  ranging from threshold to 30 MeV. Our main goal is to calculate the neutron polarization  $P_{y'}$  defined as  $P_{y'} = (\sigma_+ - \sigma_-)/(\sigma_+ + \sigma_-)$ , where  $\sigma_+$  and  $\sigma_-$  are the differential cross sections for the spin-up and spin-down neutrons, respectively, along the axis perpendicular to the reaction plane. We also calculate the total cross section as well as the differential cross section  $\sigma(\theta)$ , where  $\theta$  is the colatitude angle. Although the results for the total and differential cross sections are found to agree reasonably well with the data, the results for  $P_{y'}$  show significant discrepancy with the experiment. We comment on this discrepancy.

PACS numbers: 13.40.-f, 21.45.Bc, 24.70.+s

## I. INTRODUCTION

The induced neutron-spin polarization  $P_{y'}$  in the  $\gamma d \rightarrow \vec{n}p$  reaction is defined as  $P_{y'} = (\sigma_+ - \sigma_-)/(\sigma_+ + \sigma_-)$ , where  $\sigma_+$  and  $\sigma_-$  are the differential cross sections for the spin-up and spin-down neutron, respectively, along the axis perpendicular to the reaction plane. Conspicuous discrepancy between the experimental and theoretical values of  $P_{y'}$  is a long-standing puzzle in low-energy nuclear physics [1, 2]. Schiavilla [1] carried out an elaborate calculation of  $P_{y'}$  based on the so-called standard nuclear physics approach (SNPA). In SNPA, the nuclear wave functions are generated with the use of high-precision phenomenological nucleon-nucleon potentials that accurately reproduce thousands of neutron-proton and proton-proton scattering data (for laboratory energies below 350 MeV) along with the deuteron properties. The electromagnetic current operators in SNPA are constructed from meson-exchange diagrams in such a manner that gauge invariance and the low-energy theorems are satisfied. SNPA has been used to calculate a great many electromagnetic observables involving lightest nuclei, and its general quantitative success is well known [3, 4]. As for the  $\gamma d \rightarrow \vec{n}p$  reaction, the differential cross sections calculated by Schiavilla [1] for the lab-system photon energy,  $E_\gamma^{lab}$ , up to 30 MeV agree very well with the data. For the spin polarization  $P_{y'}$ , however, there is a large discrepancy between the state-of-the-art SNPA calculation [1] and the data. This discrepancy gives a further indication of the seriousness of the “ $P_{y'}$  puzzle”, and one is led to ask whether the problem lies with theory or experiment.

In order to shed more light on this issue, we study here the  $\gamma d \rightarrow \vec{n}p$  reaction in the framework of effective field theory (EFT). The application of EFT to nuclear electroweak processes, pioneered in Refs. [5–7], has made great progress since then with various specific approaches and techniques developed along the way. It is to be emphasized that, insofar as all the relevant low-energy constants (LECs) are known, EFT can give model-independent results, and that the accuracy of these results can be systematically assessed in virtue of the well-defined EFT expansion scheme. In the present work we study the  $\gamma d \rightarrow \vec{n}p$  reaction in the framework of pionless EFT with dibaryon fields [8–10], which has shown good convergence behavior in perturbative expansion for a number of low-energy processes in the two-nucleon systems [11–13]. We compare the results of our EFT calculation with the experimental data, and also with the theoretical results obtained in SNPA [1]. It is hoped that the present study will provide useful information regarding the  $P_{y'}$  puzzle.

This paper is organized as follows. We describe in Sec. II the basic elements such as Lagrangians, the definitions of observables, and the electromagnetic operators. In Sec. III we enumerate Feynman diagrams that appear up to the order under consideration, and evaluate their amplitudes. Sec. IV explains the relation between the amplitudes and observables. In Sec. V we show the numerical results and compare them with data as well as with the results of the previous theoretical work. Sec. VI is dedicated to conclusions.

## II. FORMALISM

As stated, we work in the framework of pionless EFT with dibaryons (dEFT for short). Since we follow the same formalism as in Ref. [10], we only give its brief summary here, relegating details to Ref. [10]. We consider two dibaryons, one in the  $^1S_0$  channel and the other in the  $^3S_1$  channel, and denote them by  $d^s$  and  $d^t$ , respectively. A dEFT Lagrangian for a case involving an external vector field is given by

$$\mathcal{L}_{\text{dEFT}} = \mathcal{L}_N + \mathcal{L}_s + \mathcal{L}_t + \mathcal{L}_{st}, \quad (1)$$

where  $\mathcal{L}_N$  is the standard heavy-nucleon Lagrangian for the one-nucleon sector;  $\mathcal{L}_s$  ( $\mathcal{L}_t$ ) is a Lagrangian for  $d^s$  ( $d^t$ ), while  $\mathcal{L}_{st}$  describes  $d^s$ - $d^t$  transition due to an external vector field (a photon field). We employ the standard counting rules and calculate the amplitude up to next-to leading order (NLO). The  $\mathcal{L}_N$  relevant to our NLO calculation reads

$$\mathcal{L}_N = N^\dagger \left[ iv \cdot D + \frac{1}{2m_N} [(v \cdot D)^2 - D^2] - i[S^\mu, S^\nu] (\mu_V f_{\mu\nu}^+ + \mu_S v_{\mu\nu}^S) \right] N, \quad (2)$$

where  $v^\mu$  is a velocity vector satisfying  $v^2 = 1$ , and  $S^\mu$  is the nucleon spin operator. Here we choose  $v^\mu = (1, \vec{0})$  and, correspondingly,  $2S^\mu = (0, \vec{\sigma})$ .  $D_\mu = \partial_\mu - \frac{i}{2}\vec{\tau} \cdot \vec{\mathcal{V}}_\mu - \frac{i}{2}\mathcal{V}_\mu^S = \partial_\mu - iQV_\mu^{\text{ext}}$  is the covariant derivative involving the isoscalar-vector and isovector-vector fields,  $Q$  is an electric charge of a nucleon and  $f_{\mu\nu}^+$  and  $v_{\mu\nu}^S$  are the isovector and isoscalar field strength tensors, respectively.  $m_N$  is the nucleon mass, while  $\mu_V = 4.706$  and  $\mu_S = 0.880$  are the isovector and isoscalar magnetic moments of the nucleon, respectively.

The dibaryon Lagrangians,  $\mathcal{L}_s$  and  $\mathcal{L}_t$ , and the transition Lagrangian,  $\mathcal{L}_{st}$ , are given by

$$\begin{aligned} \mathcal{L}_s &= -s_i^\dagger \left[ iv \cdot \mathcal{D} + \frac{1}{4m_N} [(v \cdot \mathcal{D})^2 - \mathcal{D}^2] + \Delta_s \right] s_i - y_s \left[ s_i^\dagger (N^T P_i^{(^1S_0)} N) + \text{h.c.} \right], \\ \mathcal{L}_t &= -t_i^\dagger \left[ iv \cdot \mathcal{D} + \frac{1}{4m_N} [(v \cdot \mathcal{D})^2 - \mathcal{D}^2] + \Delta_t \right] t_i - y_t \left[ t_i^\dagger (N^T P_i^{(^3S_1)} N) + \text{h.c.} \right] \end{aligned} \quad (3)$$

$$-\frac{2L_2}{m_N\rho_d}i\epsilon_{ijk}t_i^\dagger t_j B_k, \quad (4)$$

$$\mathcal{L}_{st} = \frac{L_1}{m_N\sqrt{r_0\rho_d}} \left[ t_i^\dagger s_3 B_i + \text{h.c.} \right], \quad (5)$$

$\mathcal{D}_\mu = \partial_\mu - iCV_\mu^{\text{ext}}$  is the covariant derivative coupled with the external vector field, where  $C$  is the electric charge of the dibaryon field in units of the proton charge;  $C = 2, 1$ , and  $0$  for the  $pp$ -,  $np$ - and  $nn$ -channel dibaryons, respectively.  $\Delta_s$  ( $\Delta_t$ ) is the difference between the mass of  $d_s$  ( $d_t$ ) and  $2m_N$ .  $y_s$  ( $y_t$ ) specifies the strength of  $d_s$ - $N$ - $N$  ( $d_t$ - $N$ - $N$ ) coupling.  $P_a^{(1S_0)}$  and  $P_i^{(3S_1)}$  are projectors onto the  $^1S_0$  and  $^3S_1$  two-nucleon states, respectively:

$$P_a^{(1S_0)} = \frac{1}{\sqrt{8}}\tau_2\tau_a\sigma_2, \quad P_i^{(3S_1)} = \frac{1}{\sqrt{8}}\tau_2\sigma_2\sigma_i, \quad (6)$$

where  $\tau_a$  and  $\sigma_i$  are the isospin and spin operators.  $\vec{B}$  in Eqs. (3) and (5) is the magnetic field,  $\vec{B} = \vec{\nabla} \times \vec{V}^{\text{ext}}$ , where  $\vec{V}^{\text{ext}}$  is the external vector field.  $L_1$  is a LEC representing the strength of a  $\vec{V}^{\text{ext}}$ - $d^s$ - $d^t$  vertex;  $L_2$  is a second LEC parameterizing the strength of a  $\vec{V}^{\text{ext}}$ - $d^t$ - $d^t$  vertex.  $\rho_d$  and  $r_0$  are the effective range parameters of the  $NN$  interaction for the deuteron and spin-singlet channel, respectively.

The parameters,  $\Delta_{s,t}$  and  $y_{s,t}$ , in Eqs. (3) and (4) can be fixed from the scattering length and effective range for the  $^1S_0$  and  $^3S_1$  channels. Meanwhile,  $L_1$  and  $L_2$  can be determined from the low-energy  $np \rightarrow d\gamma$  cross section and the deuteron magnetic moment, respectively. Hence there are no unknown parameters in the Lagrangian,  $\mathcal{L}_{\text{dEFT}}$ , in Eq. (1); see Ref.[10] for further details.

### III. TRANSITION AMPLITUDES

The Feynman diagrams contributing to our NLO calculation are depicted in Fig. 1. The transition amplitude  $A$ , in the center-of-mass (c.m.) frame, corresponding to diagrams (a), (b), and (c) in Fig. 1 may be written as

$$\begin{aligned} A = & \chi_1^\dagger \vec{\sigma} \sigma_2 \tau_2 \chi_2^{T\dagger} \cdot \left\{ [\vec{\epsilon}_{(d)} \times (\hat{k} \times \vec{\epsilon}_{(\gamma)})] X_{MS} + \vec{\epsilon}_{(d)} \vec{\epsilon}_{(\gamma)} \cdot \hat{p} Y_{ES} \right\} \\ & + \chi_1^\dagger \sigma_2 \tau_3 \tau_2 \chi_2^{T\dagger} i \vec{\epsilon}_{(d)} \cdot (\hat{k} \times \vec{\epsilon}_{(\gamma)}) X_{MV} \\ & + \chi_1^\dagger \vec{\sigma} \sigma_2 \tau_3 \tau_2 \chi_2^{T\dagger} \cdot \left\{ \vec{\epsilon}_{(d)} \vec{\epsilon}_{(\gamma)} \cdot \hat{p} X_{EV} + [\vec{\epsilon}_{(d)} \times (\hat{k} \times \vec{\epsilon}_{(\gamma)})] Y_{MV} \right\} \\ & + \chi_1^\dagger \sigma_2 \tau_2 \chi_2^{T\dagger} i \vec{\epsilon}_{(d)} \cdot (\hat{k} \times \vec{\epsilon}_{(\gamma)}) Y_{MS}, \end{aligned} \quad (7)$$

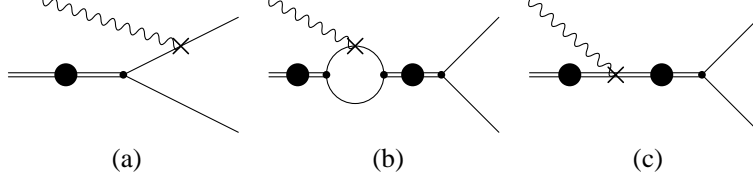


FIG. 1: Diagrams for  $d\gamma \rightarrow np$  reaction: a double line with a filled circle stands for a dressed dibaryon field, a single line for a nucleon, and a wavy line for a photon field. The photon-nucleon-nucleon vertex with “ $\times$ ” is of NLO, and the photon-dibaryon-dibaryon vertex with “ $\times$ ” is proportional to the LEC,  $L_1$  or  $L_2$ .

where  $\vec{\epsilon}_{(d)}$  and  $\vec{\epsilon}_{(\gamma)}$  are spin polarization vectors for the incoming deuteron and photon, respectively, while  $\chi_1^\dagger$  and  $\chi_2^\dagger$  are the spinors of the outgoing nucleons.  $\vec{k}$  is the momentum of an incoming photon (which is taken to be in the  $z$ -direction), and  $\vec{p}$  is the relative three-momentum of the two nucleons in the final state, and we have introduced  $\hat{k} \equiv \vec{k}/|\vec{k}|$  and  $\hat{p} \equiv \vec{p}/|\vec{p}|$ . The coefficients of the terms in Eq. (7) are given as

$$X_{MV} = -\sqrt{\frac{\pi\gamma}{1 - \gamma\rho_d \frac{1}{a_0} + ip - \frac{1}{2}r_0p^2}} \frac{1}{2m_N} \times \left\{ \mu_V \left[ \arccos\left(\frac{m_N}{\sqrt{(m_N + \frac{1}{2}\omega)^2 - p^2}}\right) + i \ln\left(\frac{m_N + \frac{1}{2}\omega + p}{\sqrt{(m_N + \frac{1}{2}\omega)^2 - p^2}}\right) \right] - \frac{\mu_V}{m_N} \left( \frac{1}{a_0} + ip - \frac{1}{2}r_0p^2 \right) F^+ + \omega L_1 \right\}, \quad (8)$$

$$X_{MS} = -\sqrt{\frac{\pi\gamma}{1 - \gamma\rho_d \gamma + ip - \frac{1}{2}\rho_d(\gamma^2 + p^2)}} \frac{1}{2m_N} \times \left\{ \mu_S \left[ \arccos\left(\frac{m_N}{\sqrt{(m_N + \frac{1}{2}\omega)^2 - p^2}}\right) + i \ln\left(\frac{m_N + \frac{1}{2}\omega + p}{\sqrt{(m_N + \frac{1}{2}\omega)^2 - p^2}}\right) \right] - \frac{\mu_S}{m_N} \left[ \gamma + ip - \frac{1}{2}\rho_d(\gamma^2 + p^2) \right] F^+ + 2\omega L_2 \right\}, \quad (9)$$

$$X_{EV} = \sqrt{\frac{\pi\gamma}{1 - \gamma\rho_d \frac{1}{m_N^2} \omega}} \frac{1}{m_N} \frac{p}{\omega} F^+, \quad Y_{ES} = \sqrt{\frac{\pi\gamma}{1 - \gamma\rho_d \frac{1}{m_N^2} \omega}} \frac{1}{m_N} \frac{p}{\omega} F^-, \quad (10)$$

$$Y_{MV} = \sqrt{\frac{\pi\gamma}{1 - \gamma\rho_d 2m_N^2}} \frac{\mu_V}{2m_N^2} F^-, \quad Y_{MS} = \sqrt{\frac{\pi\gamma}{1 - \gamma\rho_d 2m_N^2}} \frac{\mu_S}{2m_N^2} F^-. \quad (11)$$

with

$$2F^\pm = \frac{1}{1 + \frac{\omega}{2m_N} - \frac{\vec{p}\cdot\hat{k}}{m_N}} \pm \frac{1}{1 + \frac{\omega}{2m_N} + \frac{\vec{p}\cdot\hat{k}}{m_N}}, \quad (12)$$

where  $p = |\vec{p}|$ , and  $\omega$  is the incoming photon energy in the c.m. frame.

#### IV. DIFFERENTIAL CROSS SECTION AND NEUTRON SPIN POLARIZATION

We calculate the differential cross section and neutron spin polarization  $P_y'$  in the c.m. frame.<sup>1</sup> The differential cross section is given as

$$\sigma(\theta) = \frac{d\sigma}{d\Omega} = \frac{\alpha}{24\pi} \frac{pE_1}{\omega} \sum_{spin} |A|^2, \quad (13)$$

where

$$\begin{aligned} S^{-1} \sum_{spin} |A|^2 = & 16 \left( |X_{MS}|^2 + |Y_{MV}|^2 \right) + 8 \left( |X_{MV}|^2 + |Y_{MS}|^2 \right) \\ & + 12[1 - (\hat{p} \cdot \hat{k})^2] \left( |X_{EV}|^2 + |Y_{ES}|^2 \right). \end{aligned} \quad (14)$$

The symmetry factor  $S$  is equal to 2 in the present case. In Eq. (13),  $\alpha$  is the fine structure constant,  $E_1 = \sqrt{m_N^2 + p^2}$  is the energy of an outgoing nucleon in the c.m. frame, and

$$p = \frac{1}{2} \sqrt{(\omega + \sqrt{m_d^2 + \omega^2})^2 - 4m_N^2}, \quad (15)$$

where  $m_d$  is the mass of the deuteron. The total cross section is obtained by integrating Eq. (13) over the direction of  $\vec{p}$ .

To calculate the neutron spin polarization, we introduce the spin-isospin projection operator,

$$P_{\pm} = \frac{1}{2}(1 - \tau_3) \frac{1}{2}(1 \pm \vec{\sigma} \cdot \hat{n}), \quad (16)$$

where  $\hat{n}$  is the neutron spin polarization axis. We follow the convention for coordinates in [14], from which we have  $\hat{k} = (0, 0, 1)$ ,  $\hat{n} = \hat{y}' = (-\sin \phi, \cos \phi, 0)$ , and  $\hat{p} = (\sin \theta \cos \phi, \sin \theta \sin \phi, \cos \theta)$ , where  $\theta$  and  $\phi$  are the colatitude and azimuthal angles in the c.m. frame. Inserting the projection operator in the spin-isospin summation of the squared amplitude, we obtain

$$\begin{aligned} S^{-1} \sum_{spin}^P |A|^2 = & 4 \left[ |X_{MS}|^2 + |Y_{MV}|^2 - (X_{MS}^* Y_{MV} + Y_{MV}^* X_{MS}) \right] \\ & + 2 \left[ |X_{MV}|^2 + |Y_{MS}|^2 - (X_{MV}^* Y_{MS} + Y_{MS}^* X_{MV}) \right] \\ & + 3 \left[ 1 - (\hat{k} \cdot \hat{p})^2 \right] \left[ |X_{EV}|^2 + |Y_{ES}|^2 - (X_{EV}^* Y_{ES} + Y_{ES}^* X_{EV}) \right] \\ & \pm i \hat{n} \cdot (\hat{k} \times \hat{p}) \left[ (X_{EV}^* X_{MV} - X_{MV}^* X_{EV}) + (Y_{ES}^* Y_{MS} - Y_{MS}^* Y_{ES}) \right. \\ & \left. - (Y_{ES}^* X_{MV} - X_{MV}^* Y_{ES}) - (Y_{MV}^* Y_{MS} - Y_{MS}^* Y_{MV}) \right]. \end{aligned} \quad (17)$$

---

<sup>1</sup> If comparison with the experimental data necessitates it, we shall convert them into laboratory-frame quantities. Numerically, this conversion is not important in the present case.

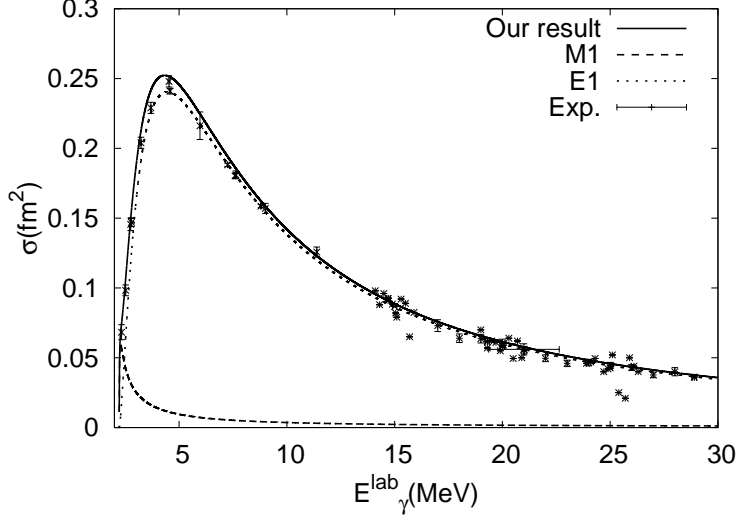


FIG. 2: Total cross section,  $\sigma$ , for the  $\gamma d \rightarrow np$  process as a function of the lab-frame photon energy  $E_\gamma^{\text{lab}}$  (MeV). The long-dashed and short-dashed lines show the M1 and E1 contributions, respectively; the solid line gives the sum of the E1 and M1 contributions. The points with error bars represent experimental data. (The experimental data are obtained from National Nuclear Data Center (NNDC) web-page [15].)

Noting that, whereas  $X_{MV}$  and  $X_{MS}$  are complex,  $X_{EV}$ ,  $Y_{MV}$ ,  $Y_{MS}$  and  $Y_{ES}$  are real, we arrive at a final form for the polarization  $P_{y'}$  as

$$\begin{aligned}
 P_{y'} &= \frac{\sigma_+(\theta) - \sigma_-(\theta)}{\sigma_+(\theta) + \sigma_-(\theta)} \\
 &= -2 \sin \theta (X_{EV} - Y_{ES}) \text{Im} X_{MV} / \left\{ 4 \left( |X_{MS}|^2 + |Y_{MV}|^2 - 2Y_{MV} \text{Re} X_{MS} \right) \right. \\
 &\quad \left. + 2 \left( |X_{MV}|^2 + |Y_{MS}|^2 - 2Y_{MS} \text{Re} X_{MV} \right) + 3(1 - \cos^2 \theta) \left( |X_{EV}|^2 + |Y_{ES}|^2 - 2X_{EV} Y_{ES} \right) \right\}.
 \end{aligned} \tag{18}$$

Since  $\hat{x}' = (\cos \theta \cos \phi, \cos \theta \sin \phi, -\sin \theta)$  and  $\hat{z}' = (\sin \theta \cos \phi, \sin \theta \sin \phi, \cos \theta)$ , one can easily verify that  $P_{x'}$  and  $P_{z'}$  vanish in the chosen coordinate system.

## V. RESULTS AND DISCUSSION

Fig. 2 shows the total cross section,  $\sigma$ , for the  $\gamma d \rightarrow np$  reaction from threshold to  $E_\gamma^{\text{lab}} = 30$  MeV. It is seen that, at low energies, there are a few data points that are off the calculated  $\sigma$  curve. We remark, however, that the error bars in the figure only represent

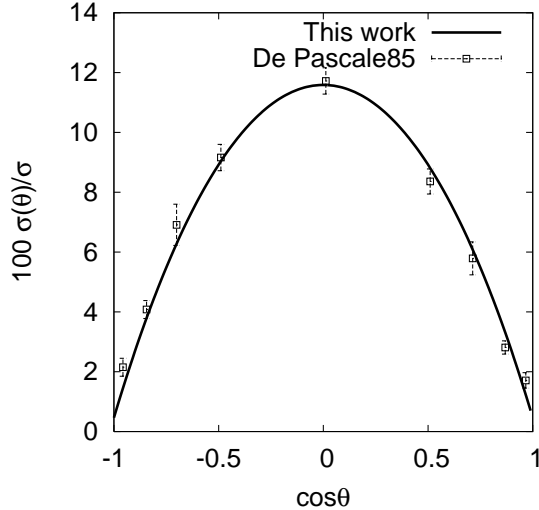


FIG. 3: Differential cross section  $100\sigma(\theta)/\sigma$  at  $E_\gamma^{lab} = 19.8$  MeV, where  $\theta$  is the scattering angle in the c.m. frame. The experimental data labeled “De Pascale85” are taken from Ref. [16].

statistical errors, and that the error bars are likely to become significantly larger when systematic errors are included. The data at higher energies,  $E_\gamma^{lab} \geq 15$  MeV exhibit some scatter, but their overall behavior is consistent with the calculated cross sections. Thus we conclude that our dEFT calculation up to NLO, which contains no adjustable parameters after the two LECs ( $L_1$  and  $L_2$ ) have been fixed, can reproduce the total cross section data reasonably well.

In Fig. 3 we plot the differential cross section  $\sigma(\theta)$  at  $E_\gamma^{lab} = 19.8$  MeV, where  $\theta$  is the scattering angle in the c.m. frame; the figure also shows the data from [16]. It can be seen that the calculated differential cross section is consistent with the measurement.

Fig. 4 shows the angular distribution of the polarization  $P_{y'}$  calculated for  $E_\gamma^{lab} = 2.75$  MeV, along with the experimental data. There are two sets of data available in the literature. One set (referred to as John61) is due to John *et al.* [17], and the other set (referred to as Jewell65) is due to Jewell *et al.* [18]. We note that John61 has significantly larger error bars than Jewell65. Fig. 4 indicates that our results agree with John61 within the large error bars except at  $\cos\theta \simeq -0.75$ . However, compared with Jewell65, the theoretical curve clearly lies below the experimental values for the entire angular range. In fact, this pattern of discrepancy between theory and experiment was already discussed in Ref. [18], where the authors used the theoretical values of  $P_{y'}$  that would turn out to be close to what we



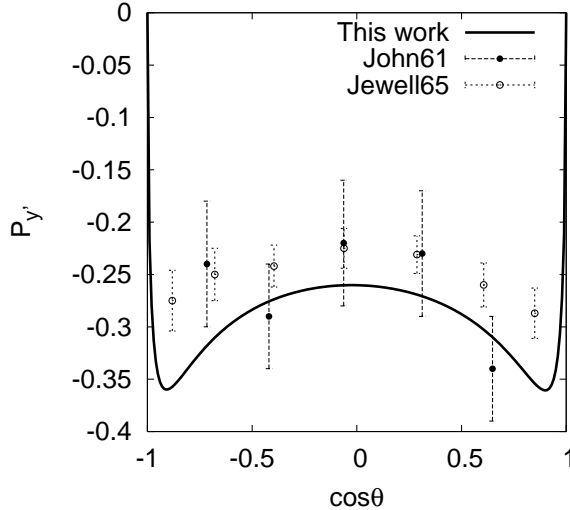


FIG. 4:  $P_{y'}$  at  $E_{\gamma}^{lab} = 2.75$  MeV plotted as a function of  $\cos\theta$ . The experimental data labeled “John61” are from [17], and those labeled “Jewell65” from [18].

have obtained here. It is to be added that  $P_{y'}$  for  $E_{\gamma}^{lab} = 2.75$  MeV calculated in SNPA [1] agrees with our results. Thus the data set Jewell65, which has much smaller error bars than the earlier set John61, disagrees with both the latest SNPA and dEFT calculations.<sup>2</sup> The persistence of the  $P_{y'}$  puzzle suggests the desirability of a new measurement of  $P_{y'}$ .

Fig. 5 shows, as a function of  $E_{\gamma}^{lab}$ , the  $P_{y'}$  for the lab-frame scattering angle  $\theta_{lab} = 45^{\circ}$  calculated in dEFT; also shown are the experimental data taken from [19]. The figure includes the results of the previous SNPA calculation [1] as well; the values labeled “IA” correspond to the impulse approximation (IA) while those labeled “MEC” include the meson exchange currents. We can see from Fig. 5 that the results of our dEFT calculation completely disagree with the data. The figure also indicates that the present dEFT calculation gives values of  $P_{y'}$  significantly different from those obtained in the SNPA calculation [1] (although, for  $E_{\gamma}^{lab} \leq 10$  MeV, the dEFT curve happens to be rather close to the IA values in [1].) Whereas the SNPA values increase almost linearly as functions of  $E_{\gamma}^{lab}$  (with the IA curve increasing more rapidly than the MEC curve),  $P_{y'}$  obtained in dEFT almost tapers off around  $E_{\gamma}^{lab} \approx 10$  MeV. This latter feature worsens the discrepancy between experiment

<sup>2</sup> We remark *en passant* that, if we multiply the calculated values of  $P_{y'}$  with a factor of about 0.7, the scaled results agree with Jewell65.

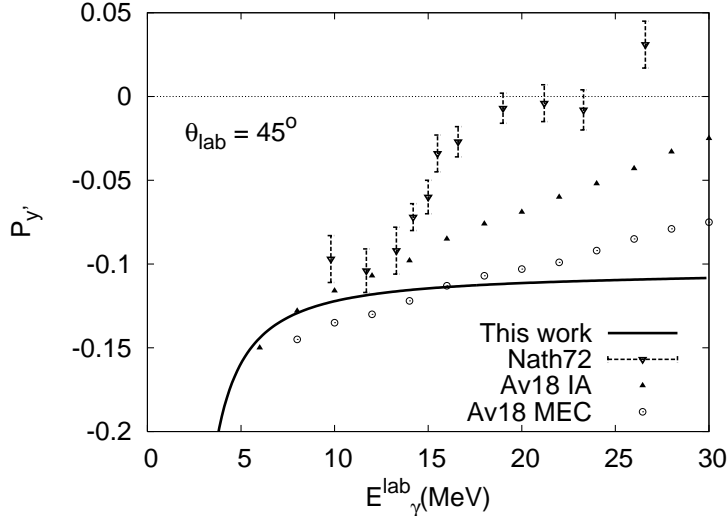


FIG. 5:  $P_{y'}$  at  $\theta_{lab} = 45^\circ$  plotted as a function of  $E_\gamma^{lab}$ , where  $\theta_{lab}$  is the scattering angle in the laboratory frame. The data labeled “Nath72” are from [19]. Filled triangles and open circles are results of IA and MEC in SNPA, respectively [1].

and theory, which was already conspicuous with the use of the SNPA values of  $P_{y'}$ .

Fig. 6 shows, as a function of  $E_\gamma^{lab}$ , the  $P_{y'}$  at  $\theta_{lab} = 90^\circ$  calculated in dEFT, together with three sets of experimental data taken from Refs. [19–21]. Comparison between theory and experiment is hampered by the fact that the data points show pronounced scatter, exhibiting at some places even inconsistencies among the data sets from the different sources. It is also curious that, for  $E_\gamma^{lab} \geq 10$  MeV, the data points show rather conspicuous oscillatory behavior. We may summarize the current situation with the statement that the average behavior of the experimental values of  $P_{y'}(\theta_{lab} = 90^\circ)$  agrees with the results of our dEFT calculation within the very large experimental uncertainties. Here again, it seems desirable to have new measurements of  $P_{y'}$ . Fig. 6 also gives  $P_{y'}$  obtained in a SNPA calculation [1]. It is seen that, within SNPA, the IA calculation always gives larger values of  $P_{y'}$  than the MEC case. The curve corresponding to our dEFT calculation lies between the IA and MEC values for  $E_\gamma^{lab} \leq 10$  MeV, but it approaches the IA results as  $E_\gamma^{lab}$  increases.

In Fig. 7, we plot the dEFT values of  $P_{y'}$  at  $\theta_{lab} = 135^\circ$ , as a function of  $E_\gamma^{lab}$ . For comparison, we also show the SNPA values of  $P_{y'}$  for the IA and MEC cases [1]. It is to be seen that, for  $E_\gamma^{lab} \leq 5$  MeV, the dEFT and SNPA results are close to each other, but that qualitative difference appears for  $E_\gamma^{lab} \geq 8$  MeV; the dEFT curve shows slow, monotonic

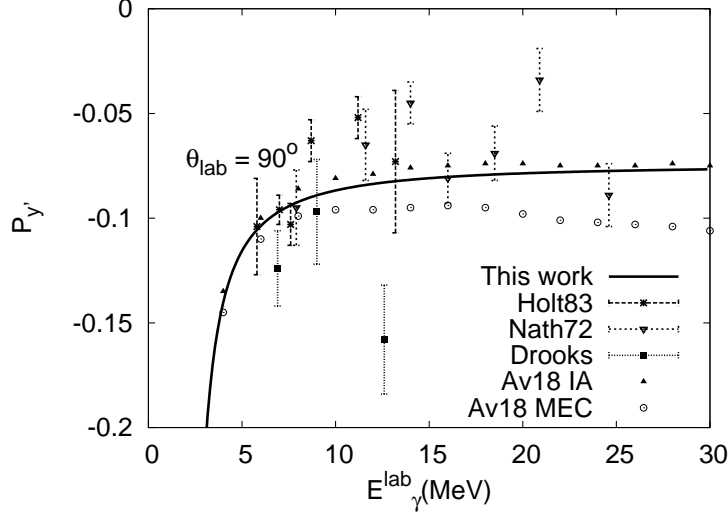


FIG. 6:  $P_{y'}$  at  $\theta_{lab} = 90^\circ$  plotted as a function of  $E_{\gamma}^{lab}$ . The data labeled “Holt83” and “Drooks” are from [20] and [21], respectively. Filled triangles and open circles are results of IA and MEC in SNPA, respectively [1].

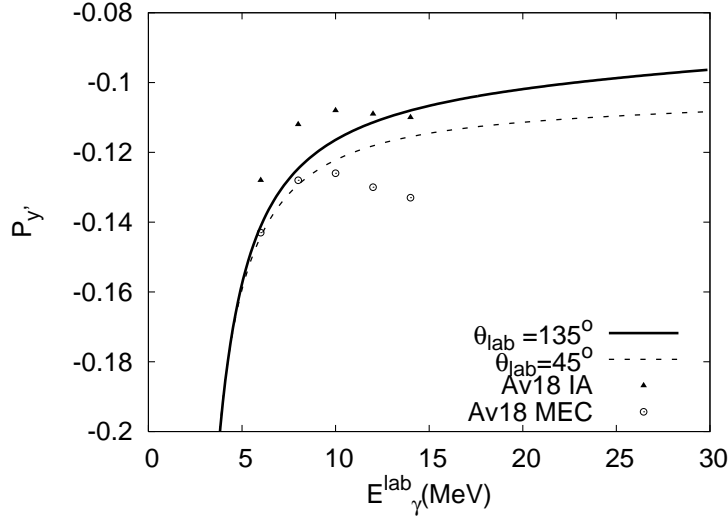


FIG. 7:  $P_{y'}$  plotted as a function of  $E_{\gamma}^{lab}$  for  $\theta_{lab} = 135^\circ$  (solid line) and  $\theta_{lab} = 45^\circ$  (dashed line). Filled triangles and open circles are results of IA and MEC in SNPA, respectively [1].

increase, whereas the SNPA results (both IA and MEC cases) start decreasing around  $E_{\gamma}^{lab} \geq 10$  MeV. We also remark that, in our dEFT calculation, the dominant contributions to  $P_{y'}$  are proportional to  $\sin \theta$  or  $\cos^2 \theta$ , which implies  $P_{y'}(\theta_{lab} = 135^\circ) \approx P_{y'}(\theta_{lab} = 45^\circ)$ . Fig. 7, which

also includes  $P_{y'}(\theta_{lab} = 45^\circ)$ , indicates that  $P_{y'}(\theta_{lab} = 135^\circ) \approx P_{y'}(\theta_{lab} = 45^\circ)$  holds rather well. By contrast, the calculation in [1] does not share this feature, another qualitative difference between our results and those in [1]. As regards comparison with experiment, because we were unable to retrieve the relevant data from the literature, we cannot make direct comparison of the theoretical  $P_{y'}(\theta_{lab} = 135^\circ)$  with experiment. However, to the extent that  $P_{y'}(\theta_{lab} = 135^\circ) \approx P_{y'}(\theta_{lab} = 45^\circ)$  holds, we can compare our theoretical curve with the data for  $P_{y'}(\theta_{lab} = 45^\circ)$  shown in Fig. 5 .

## VI. CONCLUSIONS

We have applied the pionless-EFT-with-dibaryon (dEFT) formalism to the  $\gamma d \rightarrow \vec{n}p$  reaction for the incident photon energy up to 30 MeV. As far as the total cross section and the differential cross section are concerned, the results of our dEFT calculation agree with those of the latest SNPA (standard nuclear physics approach) calculation by Schiavilla [1]. These theoretical values are in reasonable agreement with the data, which at present have appreciable uncertainties. On the other hand, for the neutron polarization  $P_{y'}$ , the results of our dEFT calculation are found to be significantly different from those obtained in SNPA [1], indicating the sensitivity of polarization observables to the theoretical frameworks used. It is noteworthy that, even if we interpret the difference between the EFT and SNPA results as a rough measure of the existing theoretical uncertainties, the “ $P_{y'}$ ” puzzle, *i.e.*, discrepancy between the theoretical and experimental values of “ $P_{y'}$ ”, still persists. Our results indicate that  $P_{y'}$  obtained in dEFT can exhibit even larger discrepancy from the data than the SNPA calculation does, for certain ranges of the scattering angle.

We remark that, at energies larger than  $E_\gamma^{lab} \sim 15$  MeV, the contributions of final-state partial waves higher than considered in our present calculation may become significant, and that the SNPA calculation [1] includes these higher partial waves. This may explain part of the differences between the dEFT and SNPA results for  $P_{y'}$ . Higher order effects within dEFT also need to be examined despite the good convergence property of dEFT found previously for many observables. It is to be noted, however, that Christlmeier and Griebhammer [22] have carried out an N<sup>2</sup>LO calculation in dEFT for the longitudinal and transverse response functions for the  $d(e, e')$  reaction. According to this work, it is highly unlikely that the large discrepancy between theory and experiment found for some of these

response functions can be ascribed to higher order terms in the dEFT expansion. A similar conclusion may hold for  $P_{y'}$ , and a calculation going up to N<sup>2</sup>LO for the  $\gamma d \rightarrow \vec{n}p$  reaction seems warranted. We also remark that, even at energies below 10 MeV, the inclusion of higher order corrections is desirable in that it will reduce theoretical uncertainties and help sharpen the issue of the discrepancy between dEFT and SNPA at low energies.

We make here a brief comment on the treatment of the internal structure of the deuteron in dEFT. The introduction of the elementary dibaryons,  $d_s$  and  $d_t$ , in dEFT might give the impression that the deuteron structure has no place in dEFT. It is to be noted, however, that a photon coupled to the intermediate nucleon (diagram (b) in Fig. 1) gives rise to momentum dependence in the deuteron form factor, and thus the structure effects subsumed in the form factor can be accommodated in dEFT. In Ref. [10], the electromagnetic form factors for the deuteron were calculated in dEFT up to N<sup>3</sup>LO, and the differential cross sections for  $e$ - $d$  elastic scattering were computed with the use of these form factors. The functions,  $A(q)$  and  $B(q)$ , that represent the momentum dependence of the cross section (see Ref. [10] for the definitions of these functions) were compared with the experimental data and also with the results of other theories, and good agreement in the low-momentum transfer region was reported. Given the generally good convergence properties of dEFT, we may expect that our present NLO calculation incorporates the bulk of the deuteron structure effects, even though a possibility does exist that  $P_{y'}$  is a “delicate” quantity that is exceptionally sensitive to higher-order terms. In this context also, an extension of the present work to higher chiral orders seems of importance.

It is worth emphasizing that the accurate understanding of polarization observables is also important in connection with parity-violating observables in nuclear electromagnetic processes [23]. In the process  $\gamma d \rightarrow \vec{n}p$ , for example, the neutron polarizations along the  $\hat{x}'$  and  $\hat{z}'$  directions vanish with the parity-conserving interactions as mentioned before, but they can be non-vanishing with the parity-violating interactions. Theoretical prediction on these parity-violation observables requires high accuracies in both the strong and electromagnetic amplitudes. A polarization observable which is sensitive to the interference between the strong and the electromagnetic amplitudes can be a good testing ground for the reliability of parity-violation calculations as well.

To summarize, our study points to the necessity of further studies, both experimental and theoretical, of the spin observables in the  $\gamma d \rightarrow np$  reaction.

## Acknowledgments

The work of SIA and CHH is supported by the Basic Science Research Program through the National Research Foundation of Korea (NRF) funded by the Ministry of Education, Science and Technology (2010-0023661). The work of YHS is supported by the US Department of Energy under Contract No. DE-FG02-09ER41621. KK's work is partly supported by the US National Science Foundation under grant number PHY-0758114.

- 
- [1] R. Schiavilla, Phys. Rev. C **72**, 034001 (2005).
  - [2] V. I. Kuklin, I. T. Obukhovskiy, V. N. Pomerantsev, A. Faessler, and P. Grabmayr, Phys. Rev. C **77**, 041001 (R) (2008).
  - [3] L. E. Marcucci, M. Viviani, R. Schiavilla, A. Kievsky, and S. Rosati, Phys. Rev. C **72**, 014001 (2005).
  - [4] L. E. Marcucci, D. O. Riska, and R. Schiavilla, Phys. Rev. C **58**, 3069 (1998).
  - [5] M. Rho, Phys. Rev. Lett. **66**, 1275 (1991).
  - [6] T.-S. Park, D.-P. Min, and M. Rho, Phys. Rep. **233**, 341 (1993).
  - [7] T.-S. Park, D.-P. Min, and M. Rho, Nucl. Phys. **A596**, 515 (1996).
  - [8] D. B. Kaplan, Nucl. Phys. **B494**, 471 (1997).
  - [9] S. R. Beane and M. J. Savage, Nucl. Phys. **A694**, 511 (2001).
  - [10] S. Ando and C. H. Hyun, Phys. Rev. C **72**, 014008 (2005).
  - [11] S. Ando, R. H. Cyburt, S. W. Hong, and C. H. Hyun, Phys. Rev. C **73**, 065501 (2006).
  - [12] S. Ando, J. W. Shin, C. H. Hyun, and S. W. Hong, Phys. Rev. C **76**, 064001 (2007).
  - [13] S. Ando, J. W. Shin, C. H. Hyun, S. W. Hong, and K. Kubodera, Phys. Lett. **B668**, 187 (2008).
  - [14] M. L. Rustgi, W. Zernik, G. Breit, D. J. Andrews, Phys. Rev. **120**, 1881 (1960).
  - [15] National Nuclear Data Center, <http://www.nndc.bnl.gov>.
  - [16] De Pascale *et al.*, Phys. Rev. C **32**, 1830 (1985).
  - [17] W. John, F. V. Martin, Phys. Rev. **124**, 830 (1961).
  - [18] R. W. Jewell, W. John, J. E. Sherwood, D. H. White, Phys. Rev. **139**, B71 (1965).
  - [19] R. Nath, F. W. K. Firk, H. L. Schultz, Nucl. Phys. **A194**, 49 (1972).

- [20] R. J. Holt, K. Stephenson, J. R. Specht, Phys. Rev. Lett. **50**, 577 (1983).
- [21] L. J. Dooks, Ph.D. thesis, Yale University, 1976 (unpublished).
- [22] S. Christlmeier and H.W. Griesshammer, Phys. Rev. C **77**, 064001 (2008).
- [23] B. Desplanques, Phys. Rep. **297**, 1 (1998).